

Systematic compositional analysis of sputter-deposited boron-containing thin films

Babak Bakhit, Daniel Primetzhofer, Eduardo Pitthan, Mauricio A. Sortica, Eleni Ntemou, Johanna Rosén, Lars Hultman, Ivan Petrov and Grzegorz Greczynski

The self-archived postprint version of this journal article is available at Linköping University Institutional Repository (DiVA):

<http://urn.kb.se/resolve?urn=urn:nbn:se:liu:diva-180132>

N.B.: When citing this work, cite the original publication.

Bakhit, B., Primetzhofer, D., Pitthan, E., Sortica, M. A., Ntemou, E., Rosén, J., Hultman, L., Petrov, I., Greczynski, G., (2021), Systematic compositional analysis of sputter-deposited boron-containing thin films, *Journal of Vacuum Science & Technology. A. Vacuum, Surfaces, and Films*, 39(6), 063408.
<https://doi.org/10.1116/6.0001234>

Original publication available at:

<https://doi.org/10.1116/6.0001234>

Copyright: American Vacuum Society

<http://www.avs.org/>



Systematic Compositional Analysis of Sputter-deposited Boron-containing Thin Films

Babak Bakhit,^{a,*} Daniel Primetzhofer,^b Eduardo Pitthan,^b Mauricio A. Sortica,^b
Eleni Ntemou,^b Johanna Rosen,^a Lars Hultman,^a Ivan Petrov,^{a,c,d} Grzegorz Greczynski^a

^a Thin Film Physics Division, Department of Physics (IFM), Linköping University,
Linköping SE-58183, Sweden

^b Applied Nuclear Physics, Department of Physics and Astronomy, Uppsala
University, Uppsala SE-75120, Sweden

^c Materials Research Laboratory and Department of Materials Science, University of
Illinois, Urbana, Illinois 61801, USA

^d Department of Materials Science and Engineering, National Taiwan University of
Science and Technology, Taipei 10607, Taiwan

Abstract

Boron-containing materials exhibit a unique combination of ceramic and metallic properties that are sensitively dependent on their given chemical bonding and elemental compositions. However, determining the composition, let alone bonding, with sufficient accuracy is cumbersome with respect to boron, being a light element that bonds in various coordination. Here, we report on the comprehensive compositional analysis of transition-metal diboride (TMB_x) thin films ($\text{TM} = \text{Ti}, \text{Zr}, \text{and Hf}$) by energy-dispersive X-ray spectroscopy (EDX), X-ray photoelectron spectroscopy (XPS), time-of-flight elastic recoil detection analysis (ToF-ERDA), Rutherford backscattering spectrometry (RBS), and nuclear reaction analysis (NRA). The films are grown on Si and C substrates by dc magnetron sputtering (DCMS) from stoichiometric TMB_2 targets and have hexagonal AlB_2 -type columnar structures. EDX considerably overestimates B/TM ratios, x , compared to the other techniques, particularly for ZrB_x . The B concentrations obtained by XPS strongly depend on the energy of Ar^+ ions used for removing surface oxides and

* Corresponding author.

Email address: babak.bakhit@liu.se (B. Bakhit)

contaminants prior to analyses and are more reliable for 0.5 keV Ar^+ . ToF-ERDA, RBS, and NRA yield consistent compositions in TiB_x . They also prove TiB_x and ZrB_x films to be homogeneous, with comparable B/TM ratios for each film. However, ToF-ERDA, employing a 36-MeV $^{127}\text{I}^{8+}$ beam, exhibits challenges in depth resolution and quantification of HfB_x due to plural and multiple scattering and associated energy loss straggling effects. Compared to ToF-ERDA, RBS (for the film grown on C substrates) and NRA provide more reliable B/Hf ratios. Overall, a combination of methods is recommended for accurately pinpointing the compositions of borides that contain heavy transition metals.

Keywords: Borides, Compositional analysis, Energy-dispersive X-ray spectroscopy (EDX), X-ray photoelectron spectroscopy (XPS), Ion beam analysis (IBA)

I. INTRODUCTION

Boron-containing materials are subject of increasing attention in a broad range of applications. Boron, B, is the lightest non-metal element with an electron in a p-orbital in its ground state. Unlike most p-elements, B hardly follows the octet rule and places six electrons into its valence shell, referred to as electron deficiency. This peculiarity has a significant influence on its chemistry, providing a high tendency to form covalent bonding.¹ In nature, B has two stable isotopes; ^{10}B (20%) and ^{11}B (80%). The ^{10}B isotope has a large neutron absorption cross section and is used as a neutron absorber in nuclear power plants.^{2,3} This isotope is also utilized in boron neutron capture therapy for cancer treatment.⁴⁻⁶ The ^{11}B isotope is, however, stable to neutron irradiation and can reduce nuclear heating, which makes it a good candidate for Mg^{11}B_2 superconductors⁷ and engineering the interfaces of multilayer supermirrors.^{8,9}

B is also an essential element in biology for the growth and maintenance of bones,¹⁰ improving wound healing,¹¹ growing higher plants,^{12, 13} boosting magnesium absorption,^{14, 15} reducing the level of inflammatory biomarkers such as high-sensitivity C-reactive protein and tumor necrosis factor,^{12, 16} raising the level of antioxidant enzymes,¹⁷ increasing the brain electrical activity, cognitive performance, and short-term memory for elders,¹⁸ and influencing on the formation and activity of key biomolecules.^{12, 13, 19} In semiconductors technology, B is used as a dopant in silicon ultra-shallow junctions with sub-10 nm size fabricated by ultra-low-energy ion implantation.^{20, 21} The performance of such small devices is determined by the distribution of implanted B dopant atoms, their electrical activation and nanostructure.^{22, 23} In addition, B has recently attracted attention for power device fabrication in the silicon carbide technology as it improves the channel mobility of metal-oxide-semiconductor field-effect transistors by incorporating into interfacial regions.^{24, 25}

Moreover, there is a class of boron-containing materials formed by mixing B and transition metals, referred to as transition-metal diborides (TMB_2), which have high melting points, excellent hardness, good tribological and corrosion properties, relatively low electrical resistivity, and high thermal and chemical stability.²⁶⁻³² TMB_2 typically crystallize in a hexagonal AlB_2 -type structure (P6/mmm, SG-191) where B atoms form graphite-like honeycomb sheets between hexagonal-close-packed TM layers. The properties of TMB_2 mainly originate from their chemical bonding; strong covalent bonding between TM and B atoms as well as within the honeycomb B sheets, and metallic bonding within TM layers.¹ Due to these ceramic and metallic features, TMB_2 thin films are promising candidates for replacing TM nitrides, which currently have a broad range of industrial applications.³⁰⁻³⁷

The properties and functionalities of the above exposé of boron-containing materials largely depend on their elemental (and impurity) compositions and distribution. Thus, a precise

compositional analysis of these materials is essential. However, accurate tracing and quantifying B by most conventional analytical techniques is typically challenging. B can be quantified by some chemistry-based analytical techniques such as potentiometric titrations,³⁸ spectrophotometric methods,³⁹ acid-base titrations in auxiliary reagents (polarimetry),⁴⁰ ion chromatography with suppressed conductivity detection,³⁸ gas chromatography,⁴¹ and inductively coupled plasma mass spectrometry.⁴² Nevertheless, these methods are time-consuming, highly prone to interferences, and require derivatization, complex analytical procedures, and several dilutions of samples.⁴²

More popular are the physics-based analytical techniques that are fast and more user friendly that can be employed for the quantitative analysis of boron-containing materials. Energy-dispersive X-ray spectroscopy (EDX) is a quick easy-to-use technique that is widely utilized for detecting and quantifying elements with $Z > 10$, with a detection limit and depth detection of > 0.5 at. % and $\leq 2 \mu\text{m}$, respectively. Despite the recent advances in their detectors enabling more accurate light-element detection, EDX still has difficulties with quantifying materials containing constituents with $Z \leq 4$, particularly in semiconductors technology, due mainly to their low characteristic photon energies.⁴³⁻⁴⁶ X-ray photoelectron spectroscopy (XPS) allows detecting elements with $Z > 2$, with an ultimate detection limit of ~ 0.1 at. %. However, XPS is a surface sensitive technique, meaning that surface oxides and hydrocarbon contaminants become a serious issue. This often requires sputter-etching the surface that apart from removing surface contaminants,⁴⁷⁻⁵² it is usually accompanied by various artifacts resulting in uncertain compositional analysis.⁵³

Secondary ion mass spectroscopy (SIMS) is a highly surface-sensitive ion beam analysis (IBA) technique that detects all elements with a detection limit of 10^{-6} at. %, which is ideal for characterizing dopants and impurities in semiconductors. Similar to XPS, this technique also relies on sputter-etching the surface due to its very low depth detection ($< 3 \text{ nm}$). In spite of the advantage

of high sensitivity and depth resolution, the quantitative analysis by SIMS is significantly complicated due to several problems such as different sputtering rates of constituent atoms, charge fractions, ion mixing by primary ions, and existence of surface oxides.⁵⁴⁻⁵⁷ Non-destructive IBA techniques such as elastic recoil detection analyses (ERDA), Rutherford backscattering spectrometry (RBS), and nuclear reaction analysis (NRA) are powerful standard-free tools for fast quantitative analysis and depth-profiling with high accuracy. Table I compares characteristic features of these methods with EDX, XPS, and SIMS. These physics-based analytical techniques are frequently used in semiconductors and thin films technologies providing reliable quantitative information (even from impurities) and depth distributions. IBA can be also combined with ion channeling to provide information about the lattice location and electrical activation of dopants, which are not possible with SIMS.²³

The motivation for this study is to critically evaluate the analysis conditions of the techniques in Table I, except SIMS, and to seek the best practice for elemental-composition determination in TMB_x . In this context, we first determine the elemental compositions of TMB_x thin films ($\text{TM} = \text{Ti}, \text{Zr}, \text{and Hf}$) grown by dc magnetron sputtering (DCMS) with EDX and XPS as two widely used analytical methods. Then, we compare results with the elemental compositions obtained from time-of-flight ERDA (ToF-ERDA), RBS, and NRA. Main challenges encountered in employing each technique for quantifying the compositions of the diborides are also discussed here.

II. EXPERIMENTAL

All films are grown in a CC800/9 CemeCon AG sputtering system equipped with rectangular $8.8 \times 50 \text{ cm}^2$ stoichiometric TMB_2 ($\text{TM} = \text{Ti}, \text{Zr}, \text{and Hf}$) targets. The targets are produced by sintering (provided by Plansee Composite Materials GmbH) with stoichiometric

mixtures of B/TM = 2 and 99.5% purity. Si(001) and C, $1.0 \times 1.0 \text{ cm}^2$, substrates are cleaned sequentially in acetone and isopropyl alcohol, and then mounted in the deposition chamber facing the target. The C substrates comprise glassy carbon with lapped and polished surface ($R_d < 50 \text{ nm}$) with bulk contaminations $< 0.01\%$. The target-to-substrate distance is 20 cm, and the system base pressure is $3.8 \times 10^{-6} \text{ Torr}$ (0.5 mPa). The growth chamber is degassed before deposition by applying 8.8 kW to each of two resistive heaters for 2 h. The total Ar (99.999% pure) pressure during deposition is 3 mTorr (0.4 Pa), and the film growth is carried out at 475 °C. A thin continuous Cr buffer layer is initially deposited on the C substrates. The TMB_x films are grown by DCMS at a target power of 3 kW and a negative dc substrate bias of 60 V.

Film thicknesses and cross-sectional morphologies from fracture cross sections are obtained by using a Zeiss LEO1550 scanning electron microscope (SEM) with an acceleration voltage of 5 kV and working distance of $\sim 3 \text{ mm}$. Deposition times are adjusted to grow the TMB_x films with two different thicknesses; a set of thick layers with a thickness of $\sim 1500 \text{ nm}$, used for microstructural evaluation and EDX compositional determination, and a set of thin layers with thicknesses of $\sim 300 \text{ nm}$, used for XPS, ToF-ERDA, RBS, and NRA measurements. θ - 2θ x-ray diffraction (XRD) scans are carried out using a Philips X'Pert x-ray diffractometer with a $\text{Cu K}\alpha$ source ($\lambda = 0.15406 \text{ nm}$) to determine crystal structure and orientation.

The elemental compositions of TMB_x thin films are obtained using EDX, XPS, ToF-ERDA, RBS, and NRA. An Oxford X-Max EDX silicon drift detector with a maximum-single-sensor-active area of 80 mm^2 , which gives high maximum throughput, low-beam-current productivity, and low-kV accuracy, coupled to the Zeiss LEO1550 SEM is used for determining the compositions. The very high throughput of counts provided by this EDX detector makes it possible to reduce quantification errors, increase analytical sensitivity, and drastically improve the

statistics of X-ray mapping.⁶⁴ The EDX instrument is intensity-calibrated using a pure Co standard sample, provided by the manufacturer, and pieces of the TMB₂ targets. Ten spectra from different area on each sample are recorded with an acquisition time of 240 s. Converting characteristic X-rays' intensities into elemental compositions in EDX analyses requires corrections on sample's atomic number (Z), absorption (A), and fluorescence excitation (F), referred to as ZAF corrections.⁴³ Here, the ZAF corrections are used in the instrument-provided software package for quantifications.

XPS measurements are carried out using a Kratos Axis Ultra DLD instrument employing monochromatic Al K_α radiation ($h\nu = 1486.6$ eV) after removing surface contaminants by sputter-etching the TMB_x thin films with an Ar⁺ ion beam. XPS measurements are performed once after sputter-etching with a 0.5-keV Ar⁺ ion beam and once after sputter-etching with a 4.0-keV Ar⁺ ion beam to examine the effect of sputter-etching Ar⁺ ion energies on the elemental quantifications. To employ similar measurement depths and be far from surfaces that have contaminants, the sputter-etching times of 3000 s and 300 s are chosen for the 0.5-keV and 4.0-keV Ar⁺ ion beams, respectively. The Ar⁺ ion beam is rastered over an area of 3×3 mm², while the acquisition area is 0.3×0.7 mm² centered in the middle of the ion-etched crater. XPS analyses are carried out using CasaXPS software.⁶⁵ The compositions are obtained by applying relative sensitivity factors (CasaXPS_KratosAxis-F1s) after excluding the spectra background using the Shirley method.⁶⁶

ToF-ERDA and RBS are carried out in a 5-MV 15SDH-2 tandem accelerator from National Electrostatic Corporation. In ToF-ERDA, recoils are detected in an angle of 45° with respect to the primary beam in a telescope measuring time-of-flight (ToF) using a foil-detector and energy in a gas ionization chamber (GIC) in coincidence. This approach results in mass resolved data in ToF-vs-Energy plots. Recoils were created using a 36-MeV ¹²⁷I⁸⁺ beam incident at 67.5° with respect to the sample surface normal. Utilizing a ToF-GIC setup provides a system with a good

energy resolution and enhanced ion species separation in terms of mass and energy, in particular for heavy species.⁶⁷ Elemental depth-profiles and average elemental compositions are obtained from ToF-ERDA time-energy coincidence spectra using two different software packages, CONTES⁶⁸ and Potku.⁶⁹ 2-MeV $^4\text{He}^+$ ions are employed for RBS measurements, and backscattered ions are detected at a scattering angle of 170° . Channeling effects in the Si substrates and potentially the textured films are minimized by adjusting the equilibrium incidence angle to 5° with respect to the surface normal and perform multiple-small-random-angular movements within a range of 2° during data acquisition. RBS spectra are simulated using SIMNRA 7.02⁷⁰ for determining the elemental compositions. One advantage of employing C substrates is the direct accessibility to the B signal, due to the low kinematic factor and scattering cross section of C. Thus, the substrate signal is not required for normalizing the particles \times solid angle products in the RBS analysis of the films, in contrast to substrates comprising elements significantly heavier than B, like Si. This permits to perform the analysis independent of the accurate knowledge of electronic stopping cross-sections of the films and substrates.

NRA is carried out in a beam line from the single stage 350 kV Danfysik implanter using a H^+ ion beam⁷¹ and scanning the beam energy in an energy range of 150 to 330 keV. Products from the $^{11}\text{B}(\text{p},\alpha)^8\text{Be}$ nuclear reaction are detected using a large-area detector with a 4- μm aluminum foil to avoid detection of backscattered protons. An additional standard detector in the chamber with a scattering angle of 167.6° allows simultaneous RBS measurements that are used for charge integration from the particles \times solid angle products. NRA cross sections used for comparison with experimental data are taken from literature⁷² and incorporated in the SIMNRA code. The stopping cross-section data used for the simulations are retrieved from the SRIM2013 code.⁷³ Systematic uncertainties of the experiment, discussed in more detail in reference⁷⁴ -- in particular for light elements, are estimated to be maximum 5-10 %, whereas statistic uncertainties

arisen from the number of experimental counts are < 2.0 %. However, the relative elemental concentrations are obtained with higher accuracy.^{75, 76}

III. RESULTS AND DISCUSSION

Cross-sectional SEM (XSEM) images of TiB_x , ZrB_x , and HfB_x thin films grown on Si(001) substrates are shown in Fig. 1. The XSEM images exhibit that all films have columnar structures. TiB_x and HfB_x layers show dense structures with smooth surfaces, while the structure of ZrB_x is less dense with a higher surface roughness. Moreover, the ZrB_x film has wider columns than the TiB_x and HfB_x films.

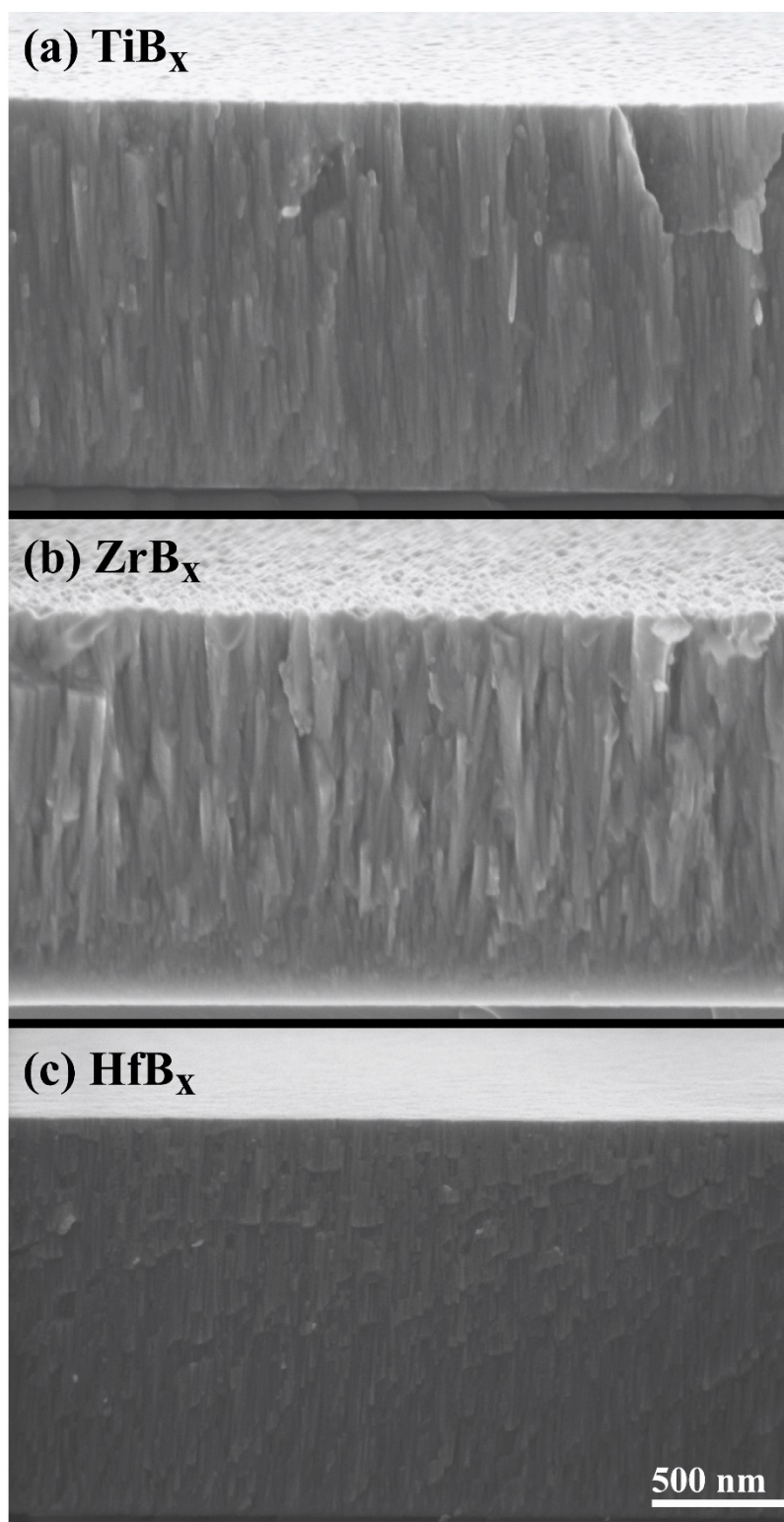


Fig. 1. Typical XSEM images of (a) TiB_x , (b) ZrB_x , and (c) HfB_x thin films grown on Si(001) substrates.

Fig. 2 shows the XRD θ - 2θ patterns of TiB_x , ZrB_x , and HfB_x thin films grown on Si(001) substrates. The peaks at 32.8° originate from the forbidden 002 substrate reflection due to multiple scattering.⁷⁷ All other reflections arise from hexagonal AlB_2 -type structure. In comparison with the TiB_x and ZrB_x films, there are significantly broader peaks in the XRD pattern of HfB_x . The full-width at half-maximum intensity of the 0001 reflection is 0.52° for TiB_x , 0.48° for ZrB_x , and 0.86° for HfB_x . The 000 l peaks of HfB_x are also asymmetric toward higher 2θ values. Preferred orientation changes from weak 000 l for TiB_x and ZrB_x to a strong one for HfB_x .

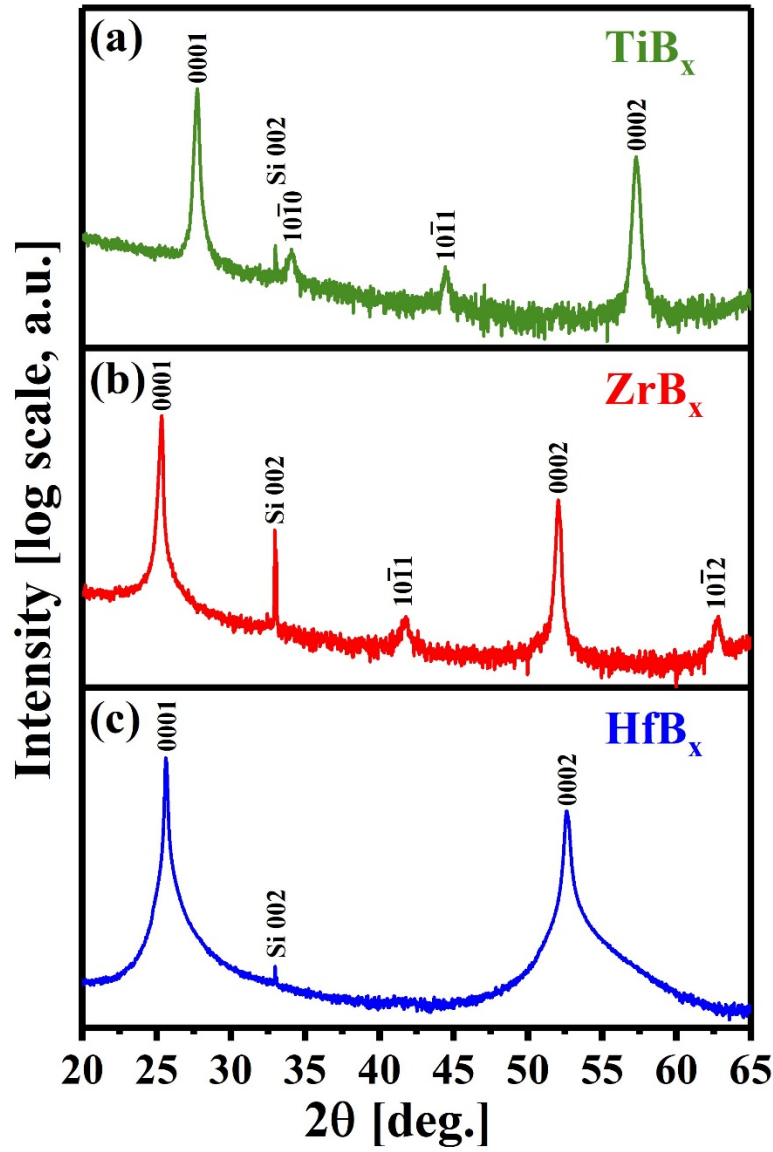


Fig. 2. XRD θ - 2θ patterns of (a) TiB_x , (b) ZrB_x , and (c) HfB_x thin films grown on Si(001) substrates.

Table II compares the relative elemental compositions of TiB_x , ZrB_x , and HfB_x films, on Si(001) substrates, determined by EDX and XPS. EDX experiments are carried out using an accelerating voltage E_{ac} of 10 kV, to avoid signals from the Si substrates, with an acquisition time of 240 s, providing adequately high signal intensities. In order to provide intense signals, which are particularly needed for quantifying materials containing light elements, the optimum E_{ac} should

be at least as twice as the excitation energy of elements.⁴³ Here, B-K (0.183 keV), Ti-L (4.509 keV), Zr-L (2.042 keV), and Hf-M (1.644 keV) characteristic X-rays are employed for quantifications. The B concentration obtained from calibrated-EDX analyses is 75 at. % for TiB_x, 79 at. % for ZrB_x, and 69 at. % for HfB_x.

As XPS is a surface-sensitive technique, samples usually require to be initially sputter-etched in order to remove surface oxides and hydrocarbon contaminants resulting from sample-air exposure.^{47, 78} However, the sputter-etching process, typically using Ar⁺ ions with energies ranging from 0.25 to 4.0 keV, is often accompanied by inducing various artifacts in the surface layer that depend on the energy and incidence angle of sputtering ions⁵³ and result in modifications of the surface chemistry and composition.⁷⁹ Changes in the surface composition depend mainly on the physical sputtering yields of components and their tendencies to form gaseous compounds (chemical sputtering), which are more related to chemical bonds than the components masses.^{80, 81} Here, we obtain the relative elemental compositions of the TMB_x thin films after sputter-etching with both low (0.5 keV) and high (4.0 keV) Ar⁺ ion energies at a constant incidence angle of 70° with respect to the sample surface normal. The 0.5-keV ion beam is used to minimize the destructive effects of Ar⁺ ion bombardment, while the 4.0-keV ion beam is used as an example of high-etch-rate XPS sputter-etching condition, often encountered in surface analysis.⁵³ Different regions on the films are selected for each measurement.

The XPS-derived elemental compositions of the TMB_x thin films sputter-etched with 0.5- and 4.0-keV Ar⁺ ions are compared in Table II. The TiB_x, ZrB_x, and HfB_x layers sputter-etched with the 0.5-keV Ar⁺ ion beam contain ~73 at. %, ~69 at. %, and ~64 at. % B, respectively. The average O concentration is ~2 at. % for TiB_x and ZrB_x, and ~1 at. % for HfB_x. The lower O concentration in HfB_x is due primarily to its highly dense microstructure. Compared to the films sputter-etched with the 0.5-keV Ar⁺ ion beam, the TMB_x layers sputter-etched with the 4.0-keV

Ar^+ ion beam appear to have less B (~ 71 at. % for TiB_x , ~ 63 at. % for ZrB_x , and ~ 58 at. % for HfB_x). The lower B concentrations in the TMB_x films sputter-etched by the 4.0-keV Ar^+ ion beam is mainly attributed to preferential B resputtering.^{53, 82-86} The difference in the B concentrations following the sputter-etching with low and high Ar^+ ion energies increases from ~ 2.8 % for TiB_x , to ~ 9.5 % for ZrB_x , to ~ 10.3 % for HfB_x . The O content of TMB_x after sputter-etching with 4 keV is in general higher than that after the 0.5-keV Ar^+ treatment and changes from ~ 3 at. % for TiB_x , to ~ 7 at. % for ZrB_x , to ~ 4 at. % for HfB_x . This observation may be explained by a forward sputtering of O triggered by high energy Ar^+ ion beam.⁸⁷

In order to evaluate the elemental distributions along the thickness of the films, the XPS depth-profiles of TiB_x , ZrB_x , and HfB_x thin films, grown on Si(001) substrates, are obtained using the 0.5-keV Ar^+ ion beam. The sputter-etching thickness of each film is estimated from determining its sputter-etching rate. Thin layers of TiB_x , ZrB_x , and HfB_x with average thicknesses of 50 nm are deposited. Then, each sample is sputter-etched to reach the Si substrate in order to determine the total time required for sputter-etching the entire film. The sputter-etching rate of each sample is finally obtained from dividing 50-nm thickness by the total sputter-etching time for each sample. The sputter-etching rate is ~ 0.68 nm/min for TiB_x and HfB_x layers, and ~ 0.79 nm/min for ZrB_x . The depth-profiles in Fig. 3 exhibit that the native oxide layer formed on the ZrB_x film is thicker than those on TiB_x and HfB_x . In addition, they clearly reveal uniform elemental distributions along the thickness of all layers.

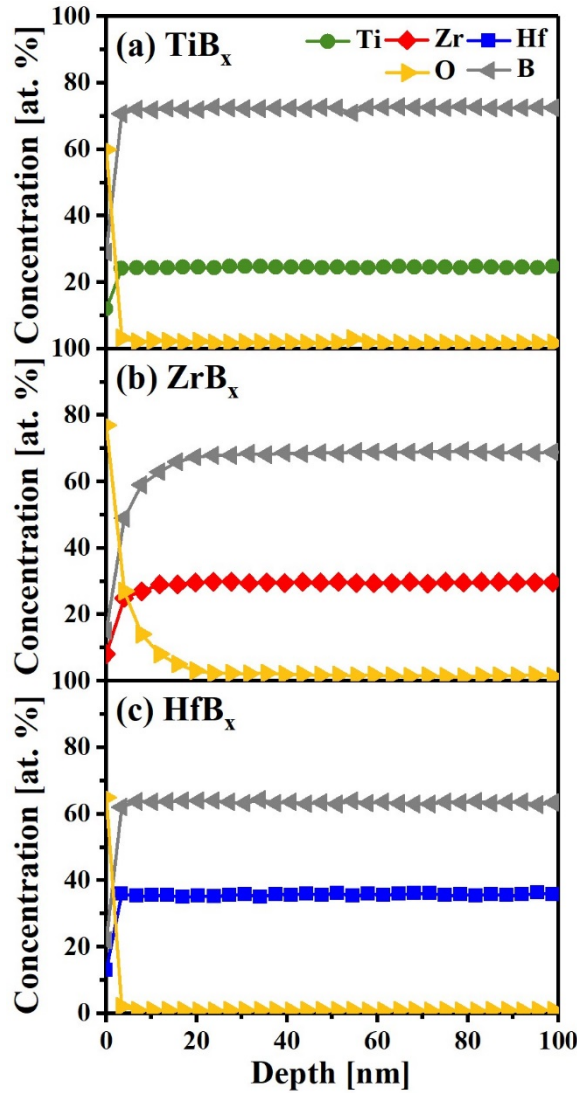


Fig. 3. XPS depth-profiles of (a) TiB_x , (b) ZrB_x , and (c) HfB_x thin films grown on Si(001) substrates, using the 0.5-keV Ar^+ ion beam.

ERDA is a widely-used IBA method with a high multi-element sensitivity, which makes it appropriate for accurately tracing and quantifying all elements, in particular light elements like H, B, C, N, and O.^{58, 60, 88} Fig. 4 exhibits the ToF-vs-Energy ERDA spectra of TiB_x , ZrB_x , and HfB_x films grown on Si(001) substrates together with their corresponding elemental depth-profiles. The dashed line in the TiB_x ToF-vs-Energy spectrum in Fig. 4(a) shows where a signal originating

from the film's top surface is expected. The ToF-vs-Energy spectra, Figs. 4(a), 4(b), and 4(c), contain signals from the films' main constituents, Si substrate, light contaminants, residual Ar from the sputter-deposition process, and scattered iodine from the incident beam. In addition, there are also some other signals that belong to transition metals in the form of homologous elements. These transition metals are impurities coming from the TMB₂ targets, with a total amount of $\leq \sim 0.5$ at. %. These elements are identified using the CONTES code that provides the ability of tracing and detecting unknown signals in ToF-ERDA spectra based on the atomic masses. The signals of ¹⁰B and ¹¹B isotopes appear very close to each other in the ToF-vs-Energy spectra. The intensities of O signals change from top surface toward the substrate, exhibiting a considerable drop from surface to the bulk film and then an increase at the film-substrate interface. The high O-signal intensities at the film-substrate interfaces are attributed to the existence of native SiO_x layers on the Si substrates. The O signal is weaker in the HfB_x spectrum than in the TiB_x and ZrB_x spectra due to its highly dense microstructure, in good agreement with XSEM images and XPS depth-profiles. The spectra also comprise signals originating from small amounts of H in the films.

The ToF-ERDA elemental depth-profiles of the TiB_x, ZrB_x, and HfB_x thin films are shown in Figs. 4(d), 4(e), and 4(f), respectively. The depth unit in ERDA codes is typically 10¹⁵ atoms/cm². In order to convert this unit to nm, the depth values are multiplied by $(1.661 \times 10^{-2} M_T) / \rho$, in which M_T is the average atomic mass of sample material, $M_T = (2M_B + M_{TM}) / 3$, in atomic mass units (amu) and ρ is the sample density in g/cm³.⁶⁰ Here, the atomic masses used for the depth unit conversions are $M_{TiB_2} = 23.16$ amu, $M_{ZrB_2} = 37.60$ amu, and $M_{HfB_2} = 66.70$ amu. The film densities are also obtained from RBS areal densities and cross-sectional SEM film thicknesses; 4.26 g/cm³ for TiB_x, 5.23 g/cm³ for ZrB_x, and 10.0 g/cm³ for HfB_x. Si concentration profiles are also included in order to approximate the position of film-substrate interfaces.

The depth-profiles clearly show the presence of native oxide layers formed on the top surface of the films. The thickness of the top-surface oxide layers is estimated to be 15 nm for TiB_x , 30 nm for ZrB_x , and 14 nm for HfB_x . Excluding the top-surface oxide layers and the regions close to the film-substrate interfaces, the plateaus observed in the elemental depth-profiles of TiB_x and ZrB_x , shown in Figs. 4(d) and 4(e), indicate uniform elemental distributions, in good agreement with XPS depth-profiles in Figs. 3(a) and 3(b). Hence, the elemental compositions of the sputter-deposited TiB_x and ZrB_x layers are depth-independent along the film thickness. However, the depth-profile of HfB_x , Fig. 4(f), does not show uniform distributions of B and Hf elements; the B concentration increases with depth, while the concentration of Hf decreases. At first glance, it might be interpreted that there is a gradient elemental composition along the HfB_x layer thickness, which is opposite to the XPS depth-profile of HfB_x that exhibits B and Hf elements are uniformly distributed as a function of depth, Fig. 3(c). In fact, the ToF-ERDA elemental composition depth-dependency observed for HfB_x mainly originates from multiple and plural scattering, referred respectively to as many small-angle and several large-angle scattering events, of primary ions and in particular heavy recoils, processes that have sufficiently large cross sections to significantly contribute at the present primary ion energies. These processes result in a considerable energy loss straggling of primary ions and heavy recoils, with reduced impact on lighter constituents.⁶⁰ To avoid these effects, higher primary ion energies can be employed, which potentially require large accelerators and higher energies deposited to the sample per detected yield.⁶¹ A more detailed explanation of this phenomenon, i.e. the breakdown of the single scattering assumption made in the analysis tools, can be found elsewhere.^{89, 90}

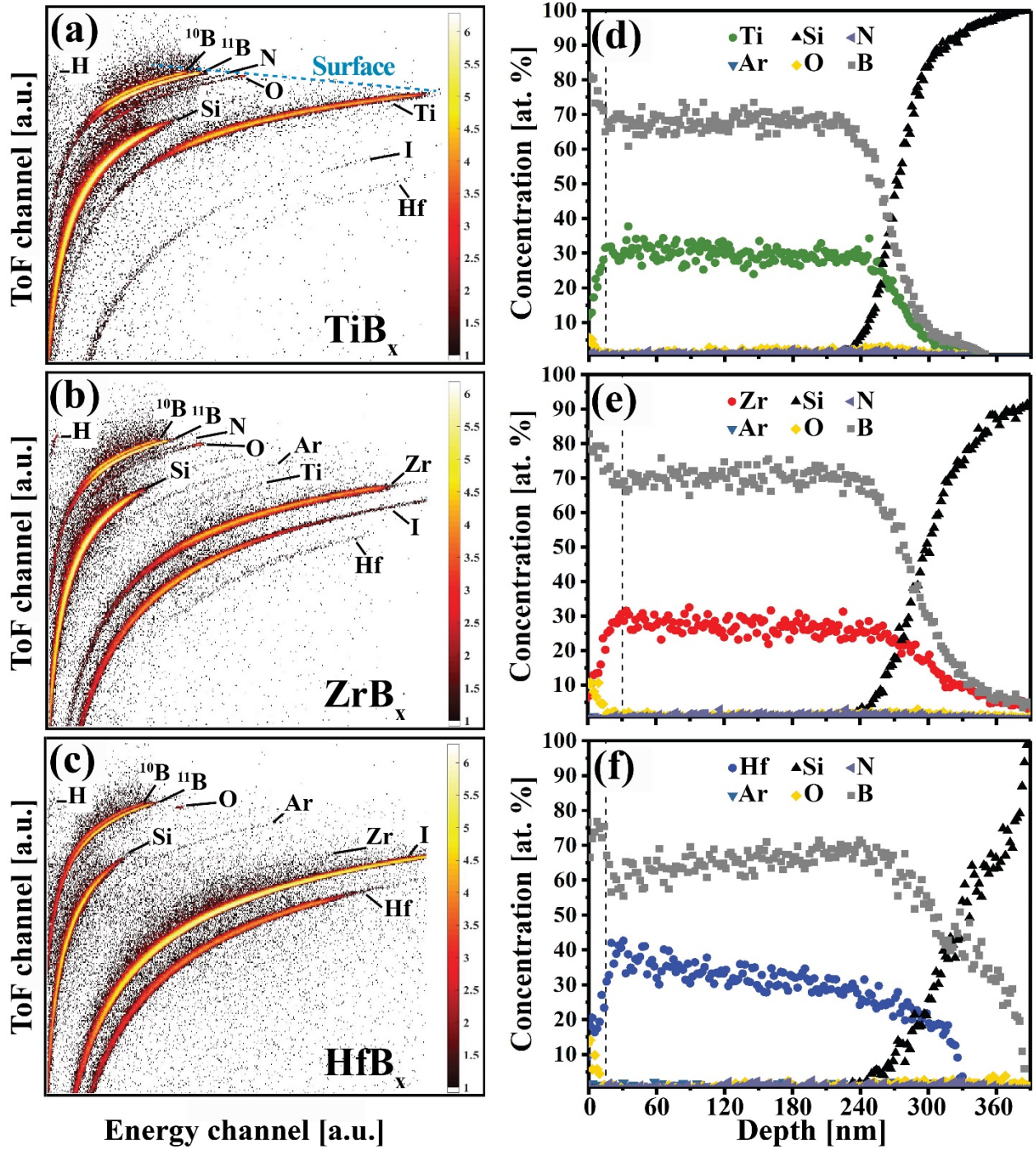


Fig. 4. ToF-vs-Energy ERDA spectra and their corresponding elemental depth-profiles of (a and d) TiB_x , (b and e) ZrB_x , and (c and f) HfB_x thin films grown on Si(001) substrates. The dashed line in the TiB_x ToF-vs-Energy spectrum shows the top surface. Thicknesses of top-surface oxide layers are marked by vertical dashed lines in the depth-profile panels.

The average ToF-ERDA elemental compositions of TiB_x and ZrB_x thin films, obtained from depths between 30 nm and 100 nm, are given in Table III. The B concentration is ~ 67.9 at. % for TiB_x and ~ 68.3 at. % for ZrB_x . The elemental composition of HfB_x in Table III is, however, determined from an area closer to the top surface, from 25 to 45 nm, in order to minimize the negative impact of multiple scattering events. This film contains ~ 60.7 at. % B and ~ 37.1 at. % Hf. The H concentration in TiB_x and HfB_x is < 0.1 at. %, while it is ~ 0.4 at. % in ZrB_x . The O concentrations in the TiB_x , ZrB_x , and HfB_x layers are ~ 0.7 at. %, ~ 0.8 at. %, and ~ 0.3 at. %, respectively, which are significantly less than those obtained by XPS. This observation can be attributed to the fact that a portion of O which is sputtered away from the surface during the XPS sputter-etching process can be redeposited on the etched surface, since it has a high affinity to form oxides, as well as the O forward sputtering effect. Thus, the XPS-derived O concentrations obtained after the sputter-etching processes are typically overestimated. The B concentrations show the highest statistic uncertainties, compared to other constituents, arising from the experimental counts of ToF-ERDA spectra with ~ 1.2 at. % for TiB_x , and ~ 1.1 at. % for ZrB_x and HfB_x .

The RBS experimental spectra (colored circles) and their corresponding SIMNRA simulations, performed for homogeneous films, (black solid curves) of TiB_x , ZrB_x , and HfB_x thin films grown on Si and C substrates are plotted in Fig. 5. The scattering cross sections of light elements are not sufficiently large in RBS to result in intense signals, especially on high Z substrates in which a high background produced from the substrate at lower energies can obscure the light-element signals.^{58, 60, 91} To observe the signals arising from the light elements, the thin films grown on C substrates are employed for the RBS measurements. A thin Cr buffer layer is initially deposited on the substrates to enhance the adhesion between the substrates and films and

to additionally shift the C-substrate signal toward lower energies in the RBS spectra. Note that in all simulations, only a single homogeneous film for the respective TMB_x system is employed, resulting in the fits shown. This observation further corroborates the interpretation of the apparent profile in the Hf concentration discussed earlier.

Fig. 5(a) shows the RBS spectra of TMB_x thin films grown on Si substrates. While the signals of the TM components (and their heavier or lighter homologues, in particular for the Zr/Hf-pair), are found to be pronounced for all TMB_x , the contribution from B is subtle. Determining the correct stoichiometry thus relies on obtaining the total incident charge from fitting the signal of the Si substrate and the evaluation of the TM concentrations from the height and area of the corresponding signals. The main sources of uncertainty in this approach are potential inaccuracies in the electronic stopping cross sections of both TMB_x compounds and Si. Input from the ToF-ERDA analyses on possible trace contaminants such as C, N, and O is used to improve the accuracy. For the films studied here, the sum of light element concentrations given in table III is ~ 2.0 at. %, which neglecting these concentrations can lead to overestimating the B concentrations by approximately the same amount.⁹²

The RBS spectra of TMB_x thin films grown on C substrates are plotted in Fig. 5(b). There is a partial overlap between Cr and Ti signals due to their close kinematic factors. Low-intensity signals appearing at channels 217 and 323 arise from O in oxide layers formed on the surface of substrate and film, respectively. The separation between B (^{10}B and ^{11}B isotopes) and C-substrate signals can be clearly observed. Data in Fig. 5(b) indicate that the concentrations of the B and TM constituents are uniform along the thicknesses of all layers, in agreement with the XPS depth-profiles in Fig. 3.

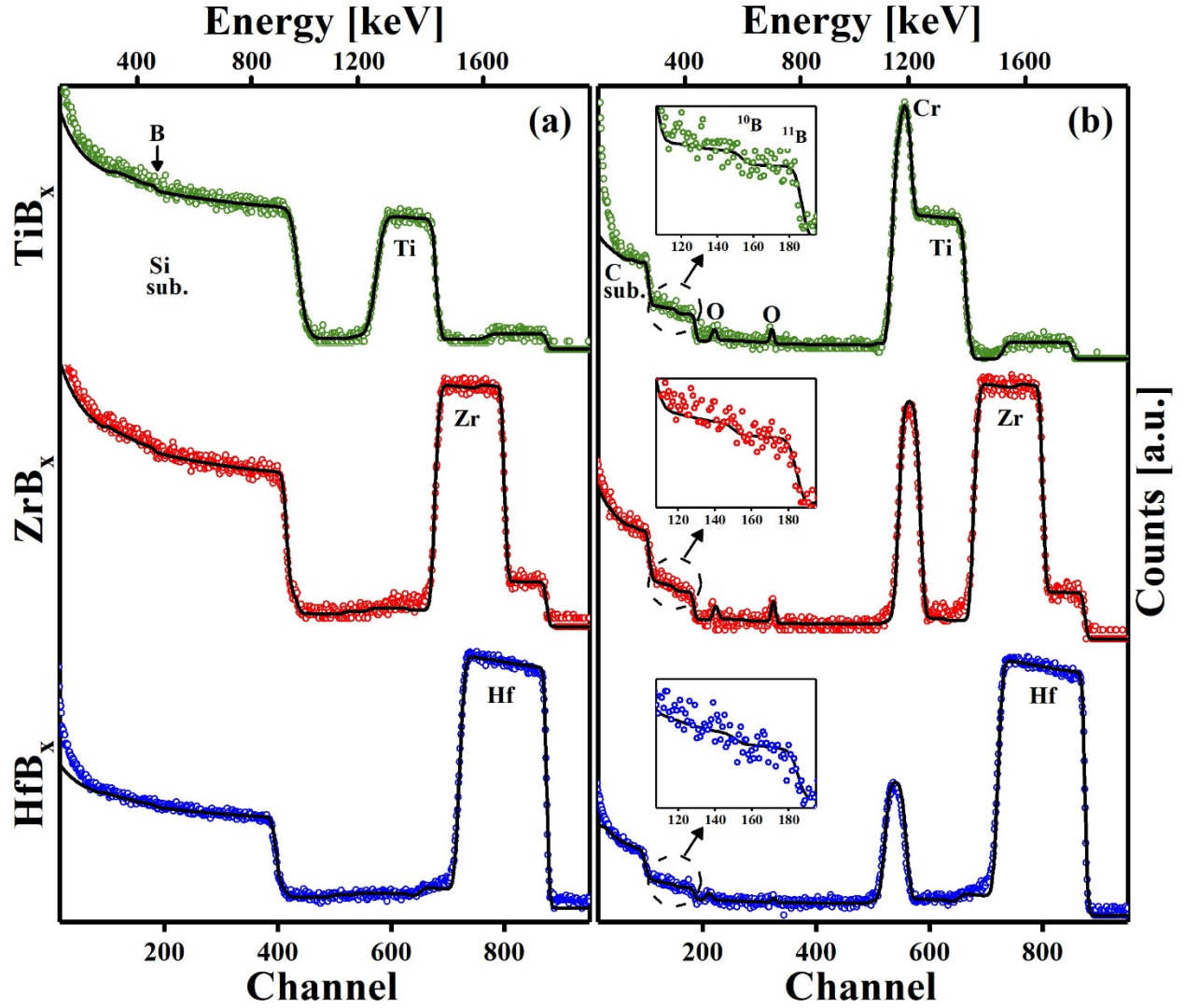


Fig. 5. RBS experimental spectra (colored circles) and SIMNRA simulations (black solid curves) of TiB_x , ZrB_x , and HfB_x thin films grown on the (a) Si(001) and (b) C substrates (sub.). The scale of vertical axis is square root. The insets in (b) show the high-resolution ^{10}B and ^{11}B signals between channels 108 and 186. The RBS spectra of ZrB_x and HfB_x thin films are simulated using correction factors (CF) on the stopping cross sections of 2-MeV $^4\text{He}^+$ ions in ZrB_2 and HfB_2 ; $\text{CF}_{\text{He}^+ \rightarrow \text{Zr}} = 0.96$ and $\text{CF}_{\text{He}^+ \rightarrow \text{Hf}} = 0.97$.

The average elemental concentrations obtained from the simulated RBS spectra of TiB_x , ZrB_x , and HfB_x layers grown on Si and C substrates are given in Table III. The concentrations of

C, N, and O obtained from the ToF-ERDA data are included in the RBS simulations. The simulated RBS spectra of TiB_x grown on the Si and C substrates yield very close elemental compositions; ~ 68.8 at. % B and ~ 29.2 at. % Ti for TiB_x on Si and ~ 68.3 at. % B and ~ 29.7 at. % Ti for TiB_x on C, which are in agreement with the concentrations derived from ERDA, see Table III.

However, simulating the RBS spectra of ZrB_x and HfB_x thin films grown on the Si and C substrates shows more pronounced differences in their elemental compositions. The RBS simulations yield that the ZrB_x film on Si contains ~ 63.8 at. % B and ~ 33.5 at. % Zr, while the film on C has ~ 69.2 at. % B and ~ 28.2 at. % Zr. In addition, the HfB_x film on Si has ~ 55.7 at. % B and ~ 41.8 at. % Hf, while this layer deposited on C consists of ~ 63.6 at. % B and ~ 34.0 at. % Hf. These deviations are mainly attributed to the imprecise electronic stopping cross sections of $^4\text{He}^+$ ions in ZrB_x and HfB_x as well as the Si substrate.^{59, 93, 94}

The SIMNRA code has a useful option in which the stopping cross sections can be modified by applying proper correction factors.⁷⁰ This option provides a good possibility to minimize the uncertainties originating from potentially imprecise electronic stopping cross sections, commonly due to the lack of available data for specific compounds. In such cases, extrapolations that are typically employed based on the Bragg's rule may not be fully accurate.^{95,}

⁹⁶ Here, we use two correction factors (CF) on the stopping cross sections of 2-MeV $^4\text{He}^+$ ions in ZrB_2 and HfB_2 ; $\text{CF}_{\text{He}^+ \rightarrow \text{Zr}} = 0.96$ and $\text{CF}_{\text{He}^+ \rightarrow \text{Hf}} = 0.97$. Both values are justified by updated extrapolated stopping cross sections for Zr and Hf.⁹⁷ Including these CF values in simulating the RBS spectra of the thin films grown on Si results in that ZrB_x contains ~ 66.4 at. % B and ~ 31.0 at. % Zr, and HfB_x has ~ 60.7 at. % B and ~ 36.8 at. % Hf. This procedure provides elemental compositions that are closer to the compositions determined from ToF-ERDA and the simulated RBS spectra of the ZrB_x and HfB_x thin films grown on the C substrates, see Table III.

The B and TM elements are also quantified from NRA measurements using a H^+ ion beam in the energy range of 150 to 330 keV, given in Table IV. The $^{11}B(p,\alpha)^8Be$ NRA has the advantage of being selective with high sensitivity to ^{11}B present in the films. By scanning the beam energy stepwise starting slightly below the energy of 163-keV resonance (width of ~ 6 keV) and by the knowledge of the nuclear reaction cross section, information on the B concentration, layer thickness, and homogeneity can be obtained in a large depth range and independent of the matrix.⁹⁰ Fig. 6 shows the experimental excitation data points (α yield vs. H^+ beam energy) and the simulated excitation curves from SIMNRA for TiB_x , ZrB_x , and HfB_x layers grown on the Si substrates with different stoichiometries. The dashed curves represent stoichiometric (B/TM = 2) simulations, while the solid curves indicate the best fit for the experimental excitation data points acquired from each film. The shape of the experimental excitation curves resembles in all cases well the simulations, indicating homogeneous compositions. Considering stoichiometric TiB_2 and ZrB_2 films with a B/TM ratio of 2, however, clearly shows discrepancies between experimental data points and simulated curves, confirming the excess B determined by other techniques. For TiB_x , a better agreement is obtained for the film containing ~ 70.6 at. % B and ~ 29.4 at. % Ti. In addition, the NRA analysis yields that the ZrB_x thin film is expected to contain ~ 72.2 at. % B and ~ 27.8 at. % Zr. However, for the HfB_x thin film, the deviation from stoichiometric HfB_2 is less pronounced, and the best simulation shows the layer consists of ~ 65.5 at. % B and ~ 34.5 at. % Hf.

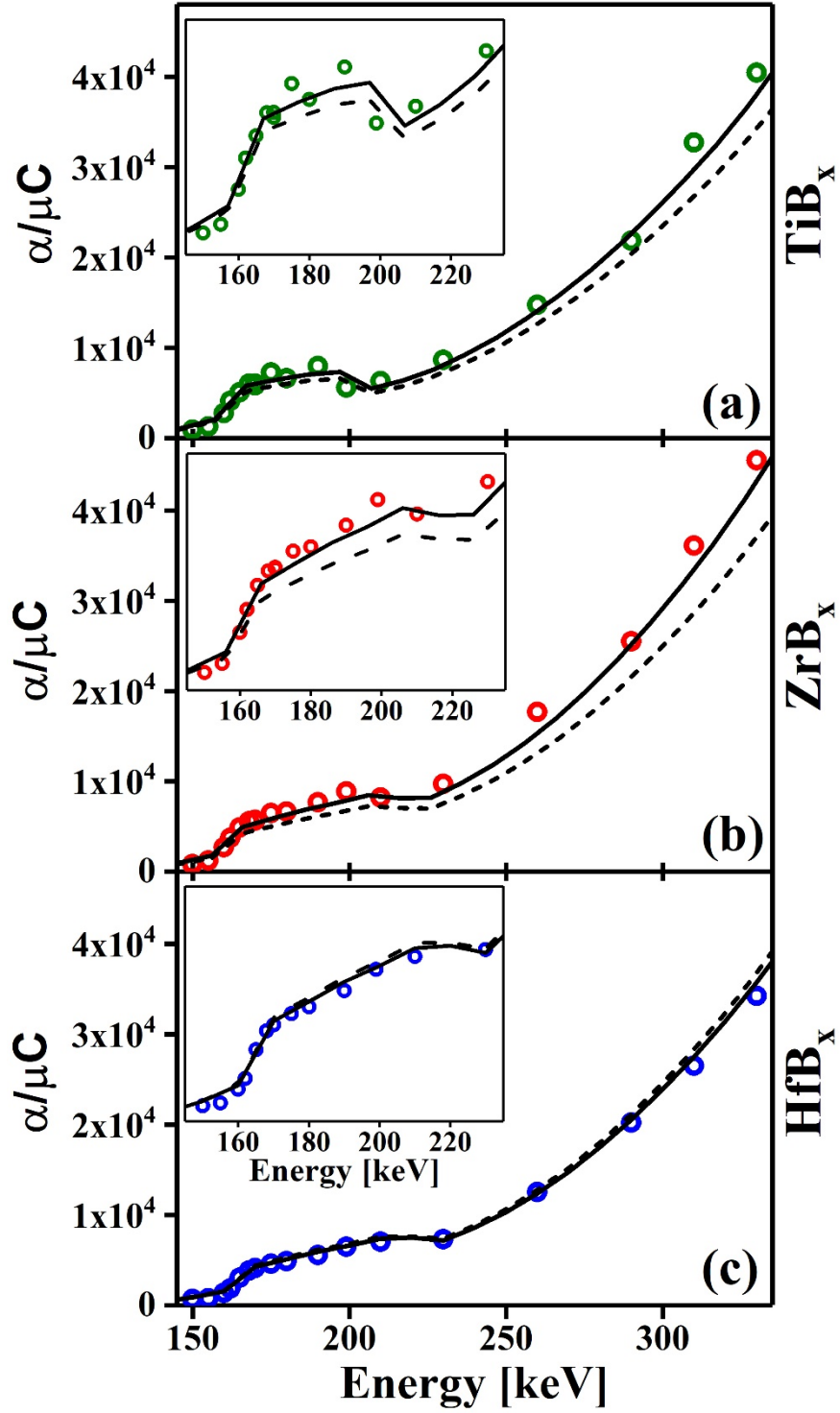


Fig. 6. $^{11}\text{B}(p,\alpha)^8\text{Be}$ NRA experimental excitation curves (colored circles) and SIMNRA simulations considering two different stoichiometries (black solid and dashed curves) for

homogeneous of (a) TiB_x , (b) ZrB_x , and (c) HfB_x thin films grown on the Si(001) substrates. The dashed curves represent simulations for stoichiometric films ($\text{B/TM} = 2$), while the solid curves indicate best fit for the experimental excitation data points acquired from each film.

Fig. 7 compares the B/TM ratios x of TiB_x , ZrB_x , and HfB_x thin films determined by EDX, XPS, ToF-ERDA, RBS, and NRA. The ratios are obtained from the elemental compositions given in Tables II, III, and IV. The x values determined by EDX are 3.0, 3.76, and 2.23 for TiB_x , ZrB_x , and HfB_x , respectively. These values are significantly higher than the values obtained by all other techniques. In general, EDX has a low analyzing power for light elements ($Z < 10$) compared to other techniques. Light elements have low-energy characteristic X-rays that are subject to strong absorption by the sample, leading to very low count rates as well as signal-to-background ratios. This effect becomes more pronounced from Ti to Hf and requires using large correction factors in determining elemental compositions that causes a decrease in the quantification accuracy.^{43, 64, 98} In addition, the electrons involved in generating the characteristic X-rays are also mainly valence electrons that take part in chemical bonding; thus, shapes and positions of the signals, which represent electron densities, may change in different compounds (possibility of systematic differences from one compound to another).^{43, 99} Thus, samples and standards need to be closely matched for best results. Moreover, detecting and quantifying light elements in compounds containing heavy elements is difficult since the energies of their characteristic X-rays typically overlap with the low-energy signals of heavy elements.^{43, 44} All these effects directly influence on both detection and quantification accuracy of TMB_x using EDX measurements.

All x values determined by XPS after sputter-etching with the 4.0-keV Ar^+ ion beam are lower than those obtained after sputter-etching with the 0.5-keV Ar^+ ion beam. For the TMB_x thin films sputter-etched with 4.0-keV Ar^+ ions, the B/TM ratio changes from 2.73 for TiB_x , to 2.10

for ZrB_x , to 1.53 for HfB_x , while this ratio is 2.92, 2.38, and 1.83 for TiB_x , ZrB_x , and HfB_x sputter-etched with 0.5-keV Ar^+ ions, respectively. This difference becomes more pronounced from $\sim 7\%$ for TiB_x , to $\sim 13\%$ for ZrB_x , to $\sim 20\%$ for HfB_x . It can be mainly attributed to the increase in the preferential resputtering effect from TiB_x to ZrB_x to HfB_x .

The x values determined from the simulated RBS spectra of TiB_x grown on the Si(001) and C substrates are very close; 2.36 and 2.30 for the film on Si(001) and C, respectively. However, there are larger differences between the x values of ZrB_x and HfB_x deposited on the Si(001) and C substrates, even after including the stopping-cross-section correction factors in the simulations. These values are 2.14 and 2.45 for ZrB_x , and 1.65 and 1.87 for HfB_x grown on Si(001) and C, respectively. These differences mainly arise from the experimental statistics of B signals, the possibility of residual ion channeling in single-crystal Si(001) substrates, and potential systematic inaccuracies in modelling multiple scattering backgrounds.

ToF-ERDA, RBS, and NRA measurements give close B/Ti ratios for the TiB_x thin film, with a maximum difference of $\sim 4\%$. The x values of ZrB_x determined by ToF-ERDA and RBS are 2.38 and 2.45 (for the film on C), respectively. However, this value is exceeded in NRA, $x = 2.6$. While ToF-ERDA, at the employed energies and using single scattering approximation, has limitations for quantifying the HfB_x thin film, giving a B/Hf ratio of 1.64, both RBS (for the film on C) and NRA indicate that this ratio is ~ 1.9 for HfB_x .

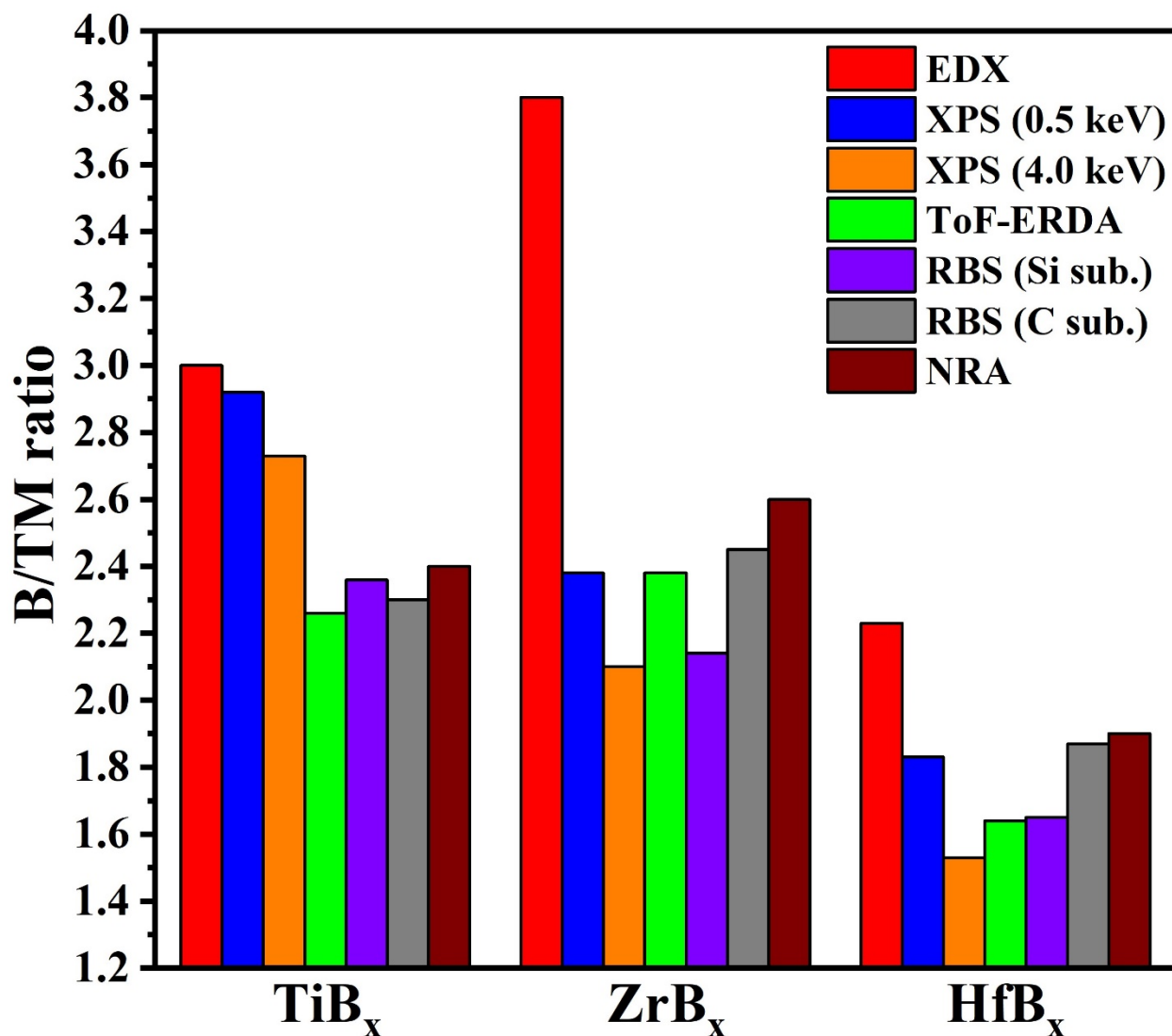


Fig. 7. B/TM ratios of TiB_x, ZrB_x, and HfB_x thin films determined by EDX, XPS, ToF-ERDA, RBS, and NRA. The ratios are obtained from the elemental compositions given in Tables II, III, and IV.

IV. CONCLUSIONS

In this work, the elemental compositions of single-phase TiB_x, ZrB_x, and HfB_x thin films are probed by EDX, XPS, ToF-ERDA, RBS, and NRA techniques. The B/TM ratios determined by EDX are considerably overestimated compared to the other methods, and are arguably less

reliable due to the presence of light B atoms that bonds in various coordination with heavy TM atoms. The compositions obtained by XPS highly depend on the sputter-etching process. The TMB_x thin films sputter-etched with 4.0-keV Ar^+ ions apparently contain less B than those sputter-etched with 0.5-keV Ar^+ ions due mainly to preferential B resputtering and induced artifacts. XPS depth-profiles using the 0.5-keV Ar^+ ion beam for sputter-etching give uniform elemental distributions along the thickness of all TMB_x thin films.

ToF-ERDA, RBS, and NRA give close x values for TiB_x . However, quantifying the elemental compositions of ZrB_x and HfB_x thin films with high levels of accuracy using IBA techniques needs precaution, depending on the technique. The elemental quantification of ZrB_x and HfB_x thin films grown on Si(001) substrates with RBS requires to include correction factors on the inaccurate electronic stopping cross sections in simulations. In agreement with XPS low-energy Ar^+ depth-profiles, ToF-ERDA, RBS, and NRA also confirm homogeneous TiB_x and ZrB_x thin films. These techniques give comparable x values for ZrB_x (after including the stopping cross-section correction factor for simulating RBS data for ZrB_x on Si). Although ToF-ERDA provides a high multi-element sensitivity (even detecting ^{10}B and ^{11}B isotopes individually), it exhibits some limitations in the depth resolution and quantification of HfB_x films. These limitations are mainly attributed to plural and multiple scattering and associated energy loss straggling effects, which become more dominant for materials consisting of elements heavier than incident ions. These issues can be to some extent resolved by employing higher energies; however, it increases required beam dose and measurement time, and such high-energy ion beams are not commonly available. Compared to ToF-ERDA, both RBS (for the film grown on C substrates) and NRA analyses give very close B/Hf ratios.

Finally, for best practice in diboride research, our results show that a careful selection of analytical techniques, depending on the specific diboride system, is required to achieve accurate

compositional analysis of boron-containing materials. It is wise to use a combination of techniques and employ calibration standards where, however, the difference in samples' microstructure may come into play. EDX and XPS should be avoided or heavily scrutinized. Ion beam analysis techniques can be to a large extent used straightforward for TiB_2 , and with elaborations also for ZrB_2 and HfB_2 . ERDA, as a stand-alone technique, is not recommended for TM diborides in which the TM element is heavier than the incident ion beam. However, it can still provide valuable information on the concentrations of light elements, obscured in other techniques.

ACKNOWLEDGMENTS

We gratefully acknowledge the financial support from the Swedish Research Council VR Grant 2021-00357, 2018-03957, and 642-2013-8020. The Knut and Alice Wallenberg (KAW) foundation for Project funding (KAW 2015.0043), the Swedish Energy Agency under project 51201-1, and Carl Tryggers Stiftelse contracts CTS 15:219, CTS 20:150, and CTS 14:431, the Swedish Government Strategic Research Area in Materials Science on Functional Materials at Linköping University (Faculty Grant SFO Mat LiU No. 2009 00971), the Swedish research council VR-RFI (#2017-00646_9) for the Accelerator based ion-technological center, and the Swedish Foundation for Strategic Research (contract RIF14-0053; for the tandem accelerator laboratory in Uppsala University) are also acknowledged.

DATA AVAILABILITY

The data that support the findings of this study are available from the corresponding author upon reasonable request.

REFERENCES

1. N. N. Greenwood and A. Earnshaw, Chemistry of the Elements, 2nd Ed., Butterworth-Heinemann, Oxford (1997).
2. V. F. Sears, Neutron news, **3**, 26 (1992).
3. R. Nikolić, A. Conway, C. Reinhardt, R. Graff, T. Wang, N. Deo and C. Cheung, Appl. Phys. Lett., **93**, 133502 (2008).
4. A. Wittig, J. Michel, R. L. Moss, F. Stecher-Rasmussen, H. F. Arlinghaus, P. Bendel, P. L. Mauri, S. Altieri, R. Hilger, P. A. Salvadori, L. Menichetti, R. Zamenhof and W. A. G. Sauerwein, Crit. Rev. Oncol. Hematol., **68**, 66 (2008).
5. J. A. Coderre and G. M. Morris, J. Radiat. Res., **151**, 1 (1999).
6. H. Koivunoro, L. Kankaanranta, T. Seppälä, A. Haapaniemi, A. Mäkitie and H. Joensuu, Radiother. Oncol., **137**, 153 (2019).
7. H. Jie, V. Luzin, M. Zaman, A. Valiyaparambil Abdulsalam, K. H. Chae, H.-i. Choi, V. Levchenko, A. Nijhuis, J. H. Kim, M. Mustapić, S. X. Dou, Y. Yamauchi, A. Khan and M. Shahriar A. Hossain, J. Am. Ceram. Soc., **103**, 5488 (2020).
8. F. Eriksson, N. Ghafoor, D. Ostach, N. Schell and J. Birch, Proc. of SPIE, Advances in X-Ray/EUV optics and components XIII, 10760, 1076006, 2018.
9. N. Ghafoor, F. Eriksson, A. Aquila, E. Gullikson, F. Schäfers, G. Greczynski and J. Birch, Opt. Express, **25**, 18274 (2017).
10. F. H. Nielsen, Nutr. Rev., **66**, 183 (2008).
11. R. M. Nzietchueng, B. Dousset, P. Franck, M. Benderdour, P. Nabet and K. Hess, J. Trace Elem. Med. Biol., **16**, 239 (2002).
12. L. Pizzorno, Integr. Med. (Encinitas), **14**, 35 (2015).
13. L. Bolaños, K. Lukaszewski, I. Bonilla and D. Blevins, Plant Physiol. Biochem., **42**, 907 (2004).
14. J. R. Stubbs, S. Zhang, P. A. Friedman and T. D. Nolin, Clin. J. Am. Soc. Nephrol., **9**, 1965 (2014).
15. I. Zofková, P. Nemcikova and P. Matucha, Clin. Chem. Lab. Med., **51**, 1555 (2013).
16. M. R. Naghii, M. Mofid, A. R. Asgari, M. Hedayati and M.-S. Daneshpour, J. Trace Elem. Med. Biol., **25**, 54 (2011).
17. R. I. Scorei, C. Ciofrangeanu, R. Ion, A. Cimpean, B. Galateanu, V. Mitran and D. Iordachescu, Biol. Trace Elem. Res., **135**, 334 (2010).
18. J. G. Penland, Biol. Trace Elem. Res., **66**, 299 (1998).
19. F. H. Nielsen, J. Trace Elem. Med. Biol., **28**, 383 (2014).
20. P. Gorai, Y. V. Kondratenko and E. G. Seebauer, J. Appl. Phys., **111**, 094510 (2012).
21. C. T. M. Kwok, R. D. Braatz, S. Paul, W. Lerch and E. G. Seebauer, J. Appl. Phys., **105**, 063514 (2009).
22. L. Lobo, B. Fernández, R. Pereiro, N. Bordel, E. Demenev, D. Giubertoni, M. Bersani, P. Hönicke, B. Beckhoff and A. Sanz-Medel, J. Anal. At. Spectrom., **6**, 542 (2011).
23. L. H. Vanamurthy, M. Huang, H. Bakhru, T. Furukawa, N. Berliner, J. Herman, Z. Zhu, P. Ronsheim and B. Doris, J. Vac. Sci. Technol. A, **31**, 031403 (2013).
24. D. Okamoto, M. Sometani, S. Harada, R. Kosugi, Y. Yonezawa and H. Yano, IEEE Electron Device Lett., **35**, 1176 (2014).
25. V. Soler, M. Cabello, M. Berthou, J. Montserrat, J. Rebollo, P. Godignon, A. Mihaila, M. R. Rogina, A. Rodríguez and J. Sebastián, IEEE Trans. Ind. Electron., **4**, 8962 (2017).
26. W. G. Fahrenholtz, G. E. Hilmas, I. G. Talmy and J. A. Zaykoski, J. Am. Ceram. Soc., **90**, 1347 (2007).

27. V. I. Matkovich, G. V. Samsonov, P. Hagenmuller and T. Lundstrom, Boron and refractory borides, Springer-Verlag, Berlin, 1977.
28. W. G. Fahrenholtz, E. J. Wuchina, W. E. Lee, Yanchun Zhou, Ultra-High Temperature Ceramics: Materials for Extreme Environment Applications, John Wiley & Sons Inc, Hoboken, New Jersey, 2014.
29. E. Sani, L. Mercatelli, D. Jafrancesco, J. L. Sans and D. Sciti, J. Eur. Opt. Soc., Rapid publ., **7**, 12052 (2012).
30. B. Bakhit, I. Petrov, J. E. Greene, L. Hultman, J. Rosén and G. Greczynski, J. Vac. Sci. Technol. A, **36**, 030604 (2018).
31. B. Bakhit, J. Palisaitis, Z. Wu, M. A. Sortica, D. Primetzhofer, P. O. Å. Persson, J. Rosen, L. Hultman, I. Petrov, J. E. Greene and G. Greczynski, Scr. Mater., **191**, 120 (2021).
32. B. Bakhit, J. Palisaitis, J. Thörnberg, J. Rosen, P. O. Å. Persson, L. Hultman, I. Petrov, J. E. Greene and G. Greczynski, Acta Mater., **196**, 677 (2020).
33. B. Bakhit, D. L. J. Engberg, J. Lu, J. Rosen, H. Högberg, L. Hultman, I. Petrov, J. E. Greene and G. Greczynski, J. Vac. Sci. Technol. A, **37**, 031506 (2019).
34. B. Bakhit, J. Palisaitis, P. O. Å. Persson, B. Alling, J. Rosen, L. Hultman, I. Petrov, J. E. Greene and G. Greczynski, Surf. Coat. Technol., **401**, 126237 (2020).
35. B. Bakhit, S. Dorri, A. Kooijman, Z. Wu, J. Lu, J. Rosen, J. M. C. Mol, L. Hultman, I. Petrov, J. E. Greene and G. Greczynski, Vacuum, **185**, 109990 (2020).
36. B. Bakhit, S. Mráz, J. Lu, J. Rosen, J. M. Schneider, L. Hultman, I. Petrov and G. Greczynski, Vacuum, **186**, 110057 (2021).
37. A. I. Bazhin, A. A. Goncharov, A. D. Pogrebnyak, V. A. Stupak and S. A. Goncharova, Phys. Met. Metallogr., **117**, 594 (2016).
38. J. J. Sciarra and J. A. Zapotocky, J. Am. Pharm. Assoc., **44**, 370 (1955).
39. F. J. López, E. Giménez and F. Hernández, Fresenius J. Anal. Chem., **346**, 984 (1993).
40. M. C. C. Azevedo and A. M. V. Cavaleiro, J. Chem. Educ., **89**, 767 (2012).
41. L.-M. Zeng, H.-Y. Wang and Y.-L. Guo, J. Am. Soc. Mass Spectrom., **1**, 482 (2010).
42. P. González, A. Sixto and M. Knochen, Talanta, **166**, 399 (2017).
43. J. I. Goldstein, D. E. Newbury, J. R. Michael, N. W. Ritchie, J. H. J. Scott and D. C. Joy, Scanning electron microscopy and X-ray microanalysis, Springer, Verlag New York, 2017.
44. J. Goldstein, D. C. Joy and A. D. Romig Jr, Principles of analytical electron microscopy, Springer Science & Business Media, New York, 2013.
45. A. J. Garratt-Reed, D. C. Bell and P. Nicholson, Energy-dispersive X-ray analysis in the electron microscope, Oxford, 2003.
46. J. C. Russ, Fundamentals of energy dispersive X-ray analysis: Butterworths monographs in materials, Butterworth-Heinemann, Oxford, 2013.
47. P. van der Heide, X-ray Photoelectron Spectroscopy: An introduction to Principles and Practices, Wiley, Hoboken, New Jersey, 2011.
48. G. Greczynski and L. Hultman, Prog. Mater. Sci., **107**, 100591 (2020).
49. D. Briggs and M. P. Seah, Practical Surface Analysis, Auger and X-ray Photoelectron Spectroscopy, Wiley, Michigan, 1990.
50. G. Friedbacher and H. Bubert, Surface and Thin Film Analysis: A Compendium of Principles, Instrumentation, and Applications, John Wiley & Sons, Hoboken, New Jersey, 2011.
51. Y. C. Lin, Y. Y. Chen, B. Y. Yu, W. C. Lin, C. H. Kuo and J.-J. Shyue, Analyst, **134**, 945 (2009).
52. M. P. Seah, S. J. Spencer, R. Havelund, I. S. Gilmore and A. G. Shard, Analyst, **140**, 6508 (2015).

53. G. Greczynski and L. Hultman, *Appl. Surf. Sci.*, **542**, 148599 (2021).
54. J. C. Vickerman and D. Briggs, *ToF-SIMS: Materials Analysis by Mass Spectrometry*, Surface Spectra, 2013.
55. C. M. Mahoney, *Cluster secondary ion mass spectrometry: principles and applications*, John Wiley & Sons, Hoboken, New Jersey, 2013.
56. P. Van der Heide, *Secondary ion mass spectrometry: an introduction to principles and practices*, John Wiley & Sons, Hoboken, New Jersey, 2014.
57. F. Stevie, *Secondary Ion Mass Spectrometry: Applications for Depth Profiling and Surface Characterization*, Momentum Press, 2015.
58. C. Jeynes and J. L. Colaux, *Analyst*, **141**, 5944 (2016).
59. M. Nastasi, J. W. Mayer and Y. Wang, *Ion beam analysis: fundamentals and applications*, CRC Press, New York, 2014.
60. Y. Wang and M. A. Nastasi, *Handbook of modern ion beam materials analysis*, Materials Research Society Pittsburgh, PA, 2009.
61. J. A. Davies, J. S. Forster and S. R. Walker, *Nucl. Instrum. Meth. B*, **136-138**, 594 (1998).
62. W. K. Chu, J. W. Mayer, M. A. Nicolet, M. A. Nicolet, *Backscattering Spectrometry*, Academic Press, Elsevier Science Technology, California, 1978.
63. H. R. Verma, *Atomic and nuclear analytical methods*, Springer, Berlin Heidelberg, 2007.
64. B. A. Carter, D. B. W. C. B. Carter, D. B. Williams, D. B. Williams and C. B. Carter, *Transmission Electron Microscopy: A Textbook for Materials Science. Diffraction. II*, Springer, New York, 1996.
65. Casa Software Ltd. (see: <http://www.casaxps.com/>).
66. D. A. Shirley, *Phys. Rev. B*, **5**, 4709 (1972).
67. P. Ström, P. Petersson, M. Rubel and G. Possnert, *Rev. Sci. Instrum.*, **87**, 103303 (2016).
68. K. S. Janson, *Conversion of Time-Energy Spectra*, Uppsala University, Sweden, 2004.
69. K. Arstila, J. Julin, M. I. Laitinen, J. Aalto, T. Konu, S. Kärkkäinen, S. Rahkonen, M. Raunio, J. Itkonen, J. P. Santanen, T. Tuovinen and T. Sajavaara, *Nucl. Instrum. Meth. B*, **331**, 34 (2014).
70. M. Mayer, W. Eckstein, H. Langhuth, F. Schiettekatte and U. von Toussaint, *Nucl. Instrum. Meth. B*, **269**, 3006 (2011).
71. S. A. Corrêa, E. Pitthan, M. V. Moro and D. Primetzhofer, *Nucl. Instrum. Meth. B*, **478**, 104 (2020).
72. E. Ligeon and A. Bontemps, *J. Radioanal. Chem.*, **12**, 335 (1972).
73. J. F. Ziegler, M. D. Ziegler and J. P. Biersack, *Nucl. Instrum. Meth. B*, **268**, 1818 (2010).
74. Y. Zhang, H. J. Whitlow, T. Winzell, I. F. Bubb, T. Sajavaara, K. Arstila and J. Keinonen, *Nucl. Instrum. Meth. B*, **149**, 477 (1999).
75. M. A. Arvizu, R.-T. Wen, D. Primetzhofer, J. E. Klemberg-Sapieha, L. Martinu, G. A. Niklasson and C. G. Granqvist, *ACS Appl. Mater. Interfaces*, **7**, 26387 (2015).
76. H.-Y. Qu, D. Primetzhofer, M. A. Arvizu, Z. Qiu, U. Cindemir, C. G. Granqvist and G. A. Niklasson, *ACS Appl. Mater. Interfaces*, **9**, 42420 (2017).
77. P. Zaumseil, *J. Appl. Crystallogr.*, **48**, 528 (2015).
78. J. F. Watts and J. Wolstenholme, *An introduction to surface analysis by XPS and AES*, John Wiley & Sons, Hoboken, New Jersey, 2003.
79. P. Sigmund, *J. Vac. Sci. Technol.*, **17**, 396 (1980).
80. R. Kelly, *Surf. Sci.*, **100**, 85 (1980).
81. A. B. Christie, J. Lee, I. Sutherland and J. M. Walls, *Appl. Surf. Sci.*, **15**, 224 (1983).
82. G. Greczynski, D. Primetzhofer and L. Hultman, *Appl. Surf. Sci.*, **436**, 102 (2018).

83. G. Greczynski, D. Primetzhofer, J. Lu and L. Hultman, *Appl. Surf. Sci.*, **396**, 347 (2017).
84. S. Oswald and R. Reiche, *Appl. Surf. Sci.*, **179**, 307 (2001).
85. R. Simpson, R. G. White, J. F. Watts and M. A. Baker, *Appl. Surf. Sci.*, **405**, 79 (2017).
86. R. Shimizu, *Nucl. Instrum. Meth. B*, **18**, 486 (1986).
87. S. Eswara, A. Pshenova, L. Yedra, Q. H. Hoang, J. Lovric, P. Philipp and T. Wirtz, *Appl. Phys. Rev.*, **6**, 021312 (2019).
88. J. R. Tesmer, C. J. Maggiore, M. Nastasi, J. Barbour and J. Mayer, *High energy and heavy ion beams in materials analysis*, Materials Research Society, Pittsburgh, US, 1990.
89. K. A. Kantre, M. V. Moro, V. Paneta and D. Primetzhofer, *Surf. Interface Anal.*, **53**, 650 (2021).
90. E. Pitthan, M. V. Moro, S. A. Corrêa and D. Primetzhofer, *Surf. Coat. Technol.*, **417**, 127188 (2021).
91. C. Jeynes, N. P. Barradas, P. K. Marriott, G. Boudreault, M. Jenkin, E. Wendler and R. P. Webb, *J. Phys. D: Appl. Phys.*, **36**, R97 (2003).
92. I. Petrov, M. Braun, T. Fried and H. E. Säterblom, *J Appl. Phys.*, **54**, 1358 (1983).
93. W.K. Chu, *Backscattering spectrometry*, Elsevier, Cambridge, Massachusetts, 2012.
94. A. Niiler, *Nucl. Instrum. Meth. B*, **24**, 358 (1987).
95. W. H. Bragg and R. Kleeman, *The London, Edinburgh, and Dublin Philosophical Magazine and Journal of Science*, **10**, 318 (1905).
96. D. I. Thwaites, *Nucl. Instrum. Meth. B*, **69**, 53 (1992).
97. M. V. Moro, P. Bauer and D. Primetzhofer, presented in part at the Interaction of Ions with the Surface, Moscow, August 19–23, 2019.
95. G. Bastin and H. Heijligers, *Quantitative electron probe microanalysis of boron in binary borides*, 2nd ed., Eindhoven University of Technology, 1986.
96. G. F. Bastin and H. J. M. Heijligers, *Scanning*, **12**, 225 (1990).

Tables:

Table I. Merits for EDX, XPS, SIMS, ERDA, RBS, and NRA techniques.

	Radiation/ Particle detection	Interaction	Elemental detection	Depth detection	Depth resolution	Typical detection limit
EDX ^{*43-46}	Characteristic X-rays	Incident electrons and target electrons	$Z > 4$	$\leq \sim 2 \mu\text{m}$	100 nm	0.5 at. %
XPS ⁴⁷⁻⁵⁰	Photoelectrons	Incident X-rays and target electrons	$Z > 2$	$\leq \sim 10 \text{ nm}$	1-5 nm	0.1 at. %
SIMS ⁵⁴⁻⁵⁷	Secondary ions	Incident ions and target atoms	All Z	$< 3 \text{ nm}$	$< 1 \text{ nm}$	10^{-6} at. %
ERDA ^{50, 58-61}	Elastic-scattered target recoils at forward angles	Incident ions and target nuclei	All Z	$\leq \sim 1 \mu\text{m}$	2-50 nm	0.01 at. %
RBS ^{50, 59, 60, 62, 63}	Elastic-scattered incident ions at backward angles	Incident ions and target nuclei	$Z > Z_{\text{ion}}$	$\leq \sim 0.5 \mu\text{m}$	2-20 nm	0.01 - 10 at. %
NRA ^{50, 59, 60, 63}	Charged particles/gamma emissions	Incident ions and target nuclei	$Z < 14$	$\leq \sim 1 \mu\text{m}$	2-20 nm	0.01 at. %

* Most instruments are not able to detect light elements ($Z \leq 4$).

Table II. Average elemental compositions of TiB_x, ZrB_x, and HfB_x thin films, grown on Si(001) substrates, obtained by EDX and XPS.

	Element (at. %)	EDX	XPS	
			0.5-keV Ar ⁺ ion beam	4.0-keV Ar ⁺ ion beam
TiB _x	B	75	73	71
	O	-	2	3
	Ti	25	25	26
	B/Ti	3.00	2.92	2.73
ZrB _x	B	79	69	63
	O	-	2	7
	Zr	21	29	30
	B/Zr	3.76	2.38	2.10
HfB _x	B	69	64	58
	O	-	1	4
	Hf	31	35	38
	B/Hf	2.23	1.83	1.53

Table III. Average elemental compositions of TiB_x , ZrB_x , and HfB_x thin films on Si and C substrates (sub.) obtained by ToF-ERDA and RBS.

Element (at. %)	TiB_x			ZrB_x			HfB_x		
	ERDA	RBS (Si sub.)	RBS (C sub.)	ERDA	RBS (Si sub.)	RBS (C sub.)	ERDA	RBS (Si sub.)	RBS (C sub.)
H	< 0.1	-	-	0.4	-	-	< 0.1	-	-
B	67.9	68.8	68.3	68.3	66.4	69.2	60.7	60.7	63.6
C	0.5	0.5	0.5	0.5	0.5	0.5	0.6	0.6	0.6
N	0.6	0.6	0.6	0.6	0.6	0.6	0.3	0.3	0.3
O	0.7	0.7	0.7	0.8	0.8	0.8	0.3	0.3	0.3
Ar	0.2	0.2	0.2	0.2	0.2	0.2	0.5	0.5	0.5
Ti	30.1	29.2	29.7	0.2	0.2	0.2	0.0	0.3	0.3
Zr	0.0	0.0	0.0	28.7	31.0	28.2	0.5	0.5	0.4
Hf	< 0.1	< 0.1	< 0.1	0.3	0.4	0.3	37.1	36.8	34.0
B/TM	2.26	2.36	2.30	2.38	2.14	2.45	1.64	1.65	1.87

Table IV. Average elemental compositions of TiB_x , ZrB_x , and HfB_x thin films, grown on the Si(001) substrates, obtained by NRA.

	B (at. %)	Ti (at. %)	Zr (at. %)	Hf (at. %)	B/TM
TiB_x	70.6	29.4	-	-	2.40
ZrB_x	72.2	-	27.8	-	2.60
HfB_x	65.5	-	-	34.5	1.90